Fermi National Accelerator Laboratory

FERMILAB-Conf-95/007-E

DØ

Design, Performance, and Upgrade of the DØ Calorimeter

Jonathan Kotcher

Fermi National Accelerator Laboratory
P.O. Box 500, Batavia, Illinois 60510

Brookhaven National Laboratory
Upton, Long Island, New York 11973

January 1995

Proceedings of the *1994 Beijing Calorimetry Symposium*, IHEP - Chinese Academy of Sciences, Beijing, China, Oct. 25-27, 1994.

Operated by Universities Research Association Inc. under Contract No. DE-AC02-76CHO3000 with the United States Department of Energy

Disclaimer

Design, performance, and upgrade of the DØ calorimeter

Jonathan Kotcher*

Physics Department, Brookhaven National Laboratory,
Upton, Long Island, New York 11973 USA

The DØ detector, located at the Fermi National Accelerator Laboratory in Batavia, Illinois, USA, is a large hermetic detector designed for the study of proton-antiproton collisions at a center-of-mass energy of 2 TeV. The calorimeter is a sampling device that employs uranium absorber and liquid argon as the active material. It has been designed for the high-precision energy measurement of electrons and jets over the full solid angle, and excellent missing transverse energy resolution for enhanced neutrino "detection". We report on some fundamental aspects of the DØ calorimeter's design and performance (the latter having been measured in both test beams and during recent data taking at the Fermilab collider), and our plan for the upgrade, which has been designed to accomodate the higher luminosities anticipated after completion of the Fermilab Main Injector.

1. INTRODUCTION

The DØ detector, located at the Fermi National Accelerator Laboratory, is a large multipurpose detector designed for the study of high mass and large transverse energy (E_T) phenomena in high energy proton-antiproton collisions. The detector stresses coverage over a large solid angle for electrons, muons, and jets, with the presence of neutrinos inferred from the measurement of missing E_T ($\not\!\!E_T$). The centerpiece of the device is hermetic uranium/liquid argon sampling calorimetry, designed to provide homogeneous, high-precision energy measurements of electrons and jets over a large range in pseudorapidity [1].

The physics program being pursued by DØ includes the search for the top quark, jet physics (including tests of quantum chromodynamics, compositeness searches, etc.), studies of the intermediate vector bosons (such as the W mass and width, vector boson self-couplings, and W/Z production in association with jets), and searches for evidence of new and exotic phenomena, including supersymmetry, fourth generation quarks, and heavy vector bosons. The detector has been accumulating collider data since May of 1992, with a total of $\approx 50\ pb^{-1}$ having been recorded to date.

This paper is organized into six sections: the introductory section contains a brief overview of the detector. The second section gives a description of the calorimeter design and its attendant trigger and electronics, along with some discussion of the design goals and how well they were met. The third section consists of a discussion of test beam results, including the results of the transfer of our absolute energy scale from the test beam to the final experiment. The fourth section contains a discussion of our experience with running the detector in collider mode: it includes a summary of the calorimeter's stability and reliability, the present status of the *in situ* calibration of the electromagnetic section, both relative and absolute, and a description of our calibration of jets. The fifth section briefly outlines our upgrade plans, and is followed by some concluding remarks.

1.1. Detector overview

Figure 1 shows a cutaway view of the detector. Moving out radially from the beam axis, there is an inner tracking volume, followed by the calorimeters and the muon system. In order to contain detector size and cost, there is no central magnetic field.

The tracking system consists of three subsystems. Immediately surrounding the beampipe is the vertex chamber, designed for the reconstruction of primary and secondary vertices. This is followed by a transition radiation detector, em-

*Representing the DØ collaboration.

ployed to enhance electron identification. The outermost tracking detectors are drift chambers, which provide charged-particle tracking and dE/dx information to $|\eta| \approx 3.2$. The calorimeters surround the tracking volume.

The muon system, consisting of five magnetized toroids together with sets of proportional drift chambers, provides momentum measurement and additional tracking information for muons with $|\eta| < 3.3$. The reader is referred to Ref. [2] for details on the overall design of the detector.

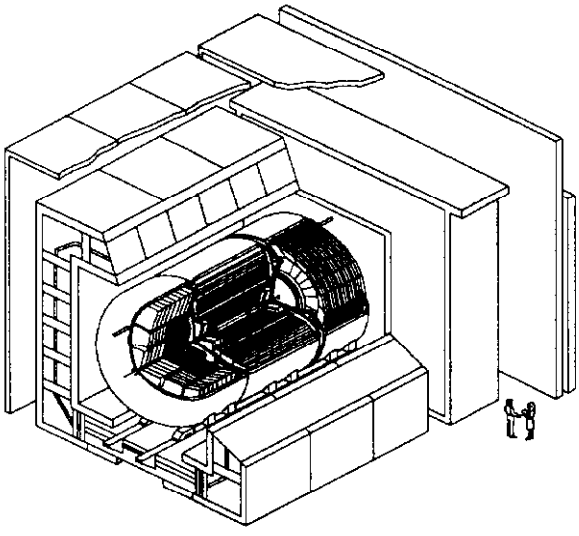

Figure 1. The DØ detector.

2. THE DØ CALORIMETERS

The calorimeters have been designed to provide excellent energy resolution over a large range in pseudorapidity. The choice of technology – liquid argon sampling alternating with, for the most part, uranium absorber – was driven by its ease of segmentation, compensation properties, stability of calibration, and homogeneity of response. The high density of uranium has also enabled us to design a compact detector that contains shower energy while reducing cost.

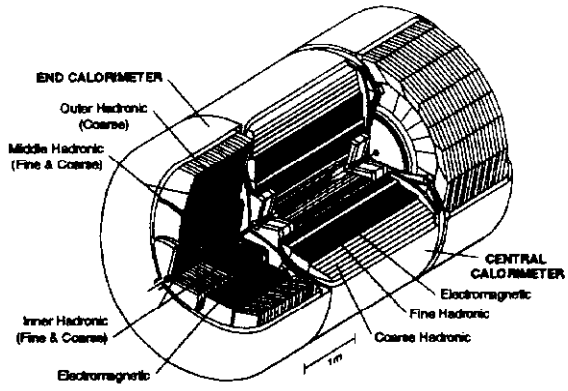

Figure 2. Cutaway view of the DØ calorimeters.

The calorimeters (see Fig. 2) are housed in three separate cryostats: a central calorimeter (CC), and two end calorimeters (EC's). Each cryostat weighs about 300 metric tons, and is filled with approximately 15,000 liters of liquid argon. The active volume is segmented into modular structures consisting of three distinct regions: the electromagnetic (EM), fine hadronic (FH), and coarse hadronic (CH) sections. The EM and FH regions employ uranium absorber; the coarse sections, which sample the tail-end of hadronic showers, consist of either copper or steel absorber.

The CC is cylindrically shaped, with the absorber plates oriented parallel to the $\bar{p}p$ beam axis. The modules are trapezoidal in cross section, and are nested in three concentric rings. The EM section is closest to the beam axis, followed by the FH and CH regions. The EM section consists of 32 modules, each subtending 0.2 radians in azimuth (ϕ). The FH and CH sections are each comprised of 16 modules. All CC modules are approximately 250 cm in length.

The absorber plates in the EC's are oriented perpendicular to the beam axis. The EM section in each end calorimeter consists of one module that is situated on the innermost face of the EC module array, and covers the full azimuth and $1.4 < |\eta| < 4.1$ [3]. The inner hadronic module, which consists of both a fine and a coarse section, is directly behind the EM module. It

Table 1
Some detector parameters

Property	Electromagnetic	Fine Hadronic	Coarse Hadronic
Absorber	Uranium	Uranium	Copper/Steel
Plate Thickness (mm)	3.0(CC)/4.0(EC)	6.0	46.5
Section Thickness	$21X_0$	3.3-4.7λ_0	3.2-7.0λ_0
Number of Unit Cells	21	50-65	9-16
Longitudinal Readout Segmentation	4 times (2,2,7,10X_0)	3-4 times	1-3 times
Pedestal width (MeV)	5-20	10-70	25-100
Cell Capacitance (nF)	0.3-1.5	3.0-5.0	3.0-4.0

Radiation (interaction) lengths are denoted by X_0 (λ_0).

subtends $1.6 < |\eta| < 5.2$ as well as the full range in ϕ. The inner hadronic module is surrounded by two concentric rings of modules: the middle hadronic ring (consisting of both a fine and a coarse section), and the outer hadronic section (coarse only). Each of these rings consists of 16 modules.

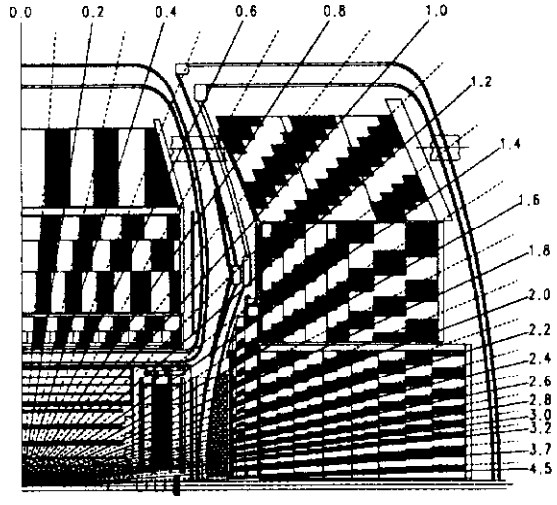

Figure 3. Schematic side view of the central and one end calorimeter. The shaded areas indicate the longitudinal and transverse readout pattern, and the rays are lines of constant pseudorapidity.

The total thickness of the calorimeter varies from about 7 to 9 interaction lengths (λ_0), depending on pseudorapidity. In addition to improving the jet resolution by containing hadronic showers, the large amount of material helps to limit hadronic punch-through to the outer muon system. The calorimeter readout is arranged into $\approx 2,500$ semi-projective towers of size 0.1×0.1 in $\Delta\eta \times \Delta\phi$. In order to enhance position resolution for electrons and photons, the transverse readout segmentation at electromagnetic shower maximum (EM readout layer 3) is twice as fine in each dimension (0.05×0.05). Figure 3 shows a side view of a portion of the DØ calorimeters, showing both the longitudinal and transverse segmentation pattern. Table 1 summarizes some of the detector parameters.

In order to improve the energy resolution for particles that traverse the inter-cryostat region ($0.8 < |\eta| < 1.4$), both "massless gaps" and an inter-cryostat detector have been added. The "massless gaps", so named because they contain no absorber material, are located between the modules and the cryostat in the liquid. They sample the shower energy that is lost by particles that traverse the module endplates and cryostat walls. The inter-cryostat detector, located between the cryostats in the η region defined above, consists of scintillator tiles that play a similar role.

Individual modules consist of repeating sections of unit cells such as those shown in Fig. 4, which shows a longitudinal section through a typical module. The absorber plates vary in thickness and composition in the different calorimeter regions; the gap spacing between the signal boards and the absorber plates is 2.3 mm throughout. The substrate for the signal boards

is composed of G-10, which is coated with a carbon-loaded resistive epoxy to which 2.0 kV high voltage is applied. With the absorber plates at ground potential, this provides the drift field for ionization across the gap. The charge collection time is ≈ 450 *ns*. In between the two layers of G-10 are etched copper pads, on which signals are capacitively induced by charge drifting across the gap. The G-10 plays the role of a blocking capacitor between the preamplifiers and the high voltage.

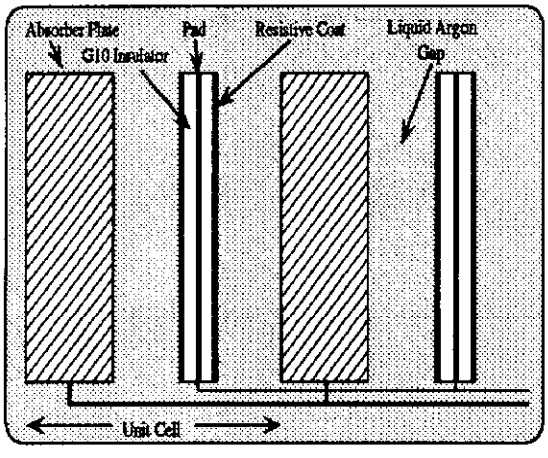

Figure 4. Typical unit cell for the calorimeter, showing the gap structure, the grounded absorber plates, and the signal boards.

The signals are locally ganged (longitudinally) before being directed to the periphery of the modules via multi-layer boards. The details of the ganging depend on the particular location in the calorimeter. The signals are then sent to the exterior of the calorimeter via 30Ω coaxial cable to preamplifiers housed in boxes atop the cryostats. After amplification and integration, the signals are brought below the detector platform to signal shapers. In addition to performing unipolar shaping, the shapers sample the signal voltage just prior to (the "baseline") and 2.2 μs after (signal "peak") the $\bar{p}p$ crossing. The baseline is then subtracted from the peak voltage to obtain the final analog signal. In order to reduce the dynamic range requirements of the digitization that follows, the shaper outputs can be amplified by 1 or by 8, depending on the size of the resulting signal.

Provided a first-level trigger has been fired (see below), the shaper output is multiplexed to analog-to-digital converters (ADC's) that have 12-bit resolution and 15-bit dynamic range. Upon receiving an appropriate signal from the software trigger, the data is then shipped to a host computer to be recorded. There are a total of 47,800 readout channels for all three cryostats.

Hodoscopes mounted on the inner faces of the two end cryostats provide the initial trigger, indicating that an inelastic proton-antiproton collision has taken place. The $\approx$ 100-200 *kHz* interaction rate is reduced to about 150 *Hz* by a hardware trigger, which utilizes both muon and calorimeter information. The calorimeter trigger is based on the energy measured in trigger towers of size 0.2×0.2 in $\Delta\eta \times \Delta\phi$, which is obtained by making appropriate sums of fast pickoffs at the shaper inputs. The calorimeter energy signal is converted to E_T, and first-level decisions are based on various combinations of electromagnetic and hadronic E_T, total scalar E_T, and $\not\!\!E_T$. The second-level trigger consists of a series of μVAX nodes, each of which contains software for event reconstruction. More precise determinations of relevant event quantities (electrons, jets, etc.) are made here, whereupon candidate events satisfying appropriate filtering criteria are passed on to be recorded. The output rate of this trigger is of the order of 3 *Hz*, and is dictated by the rate at which events can be recorded by the host computer. An event consists of about 400-500 kBytes of data, representing $\approx 120,000$ readout channels for the entire detector. The reader is directed to Ref. [4] for more details on the calorimeter trigger.

2.1. Some Electronics Benchmarks

A minimum ionizing particle liberates $\approx$ 20,000 electrons in the argon as it traverses a $2.3 \times 2 = 4.6$ *mm* gap. This corresponds to $\approx$ 1 MeV of energy deposited, or 3 *fC* of charge. In our system, this is equal to about 4 ADC counts. The least

ADC count in the calorimeter thus corresponds to roughly 5,000 electrons deposited in the active material. The 15-bit dynamic range of our ADC's gives a full range for each channel of $\approx$ 32,700 ADC counts.

Because of the large number of small signals that are brought out of the calorimeter, much attention was paid during the design and fabrication of the detector to keeping coherent noise at a low level. Since E_T flow is a crucial event variable at hadron colliders (at both the trigger and overall event reconstruction level), relatively small amounts of localised coherence in the detector could significantly degrade our physics capability. From *in situ* measurements performed prior to beam delivery, we found that we were able to sum the coherent noise in 4,000 channels before the total coherent noise was equal to the incoherent noise: the per-channel coherent noise is, on average, less than 2% of the incoherent contribution. This is quite good; coherent noise is not a problem at DØ.

During commissioning of the central calorimeter, we studied the response of the calorimeter to cosmic ray muons [5]. Minimium ionizing signals are seen well above the noise in all layers of the calorimeter. The ratio of the average muon signal in a given depth to its pedestal *r.m.s.* width is approximately 7:1 (this depends on the depth, and is a typical value). Typical cell capacitances in each of the calorimeter sections, as well as representative pedestal widths, are given in Table 1. In the EM and FH sections, the pedestal widths are dominated by the random noise associated with uranium decays.

3. TEST BEAM RESULTS

The performance of subsets of both the CC and the EC modules was evaluated in test beams at Fermilab, with some of the information having been carried over directly for use in the main experiment. The following describes some results from those tests.

3.1. Sampling weights

Using electron data from the test beam, we have carried over sampling weights for the electromagnetic section. The method involves minimizing the following χ^2:

$$\chi^2 = \sum_{\eta} \sum_{p} \sum_{i=1}^{N} \left(\frac{p_i - E_i}{\sigma_i} \right)^2 . \qquad (1)$$

The quantity p_i is the beam momentum for the i^{th} event as determined from bending magnets in the beam line, E_i is the reconstructed calorimeter energy (described below), and σ_i is the calorimeter energy resolution for electrons at momentum p_i. In order to obtain weights that are optimised uniformly over the available momentum range, we sum over an equal number of events at each momentum setting in the range 10 to 150 GeV/c. For CC, where the angle of incidence of the particle with respect to the absorber plates varies considerably for particles produced at the nominal interaction point, we perform this sum over three η regions. For the end calorimeters, where the range of incident angles is significantly smaller, we use only one η position.

The reconstructed calorimeter energy on the i^{th} event, E_i, is given by:

$$E_i = \alpha \sum_{j=1}^{5} \beta_j E'_{ji} + \delta. \qquad (2)$$

Here, α is an overall ADC-to-GeV conversion, β_j is the sampling weight for the j^{th} calorimeter layer, and E'_{ji} is the calorimeter energy (in ADC counts) read out in the j^{th} layer on the i^{th} event. Delta (δ) is an energy- and η-independent offset. We obtain the α, β_j, and δ for which the χ^2 given in Eq. 1 is minimised. The sum in Eq. 2 is over five calorimeter layers: the four electromagnetic, and the first fine hadronic layer. By convention, we fix the third electromagnetic layer to unity.

This procedure was performed independently for CC and EC. The appropriate series of constants were carried over from the test beam to DØ for each cryostat type independently.

For all hadronic layers, we use sampling weights that are calculated from our knowledge of dE/dx energy loss in the module material, using known module parameters (G-10, absorber thickness, copper cladding, gap widths, etc.) as input.

3.2. Detector performance

Of fundamental interest is the response of the modules to high voltage. The response to 100 GeV electrons in the end calorimeter EM module as a function of high voltage is shown in Fig. 5. It will be noticed that small fluctuations in voltage at 2 kV, our operating voltage, induce a small associated change in module response.

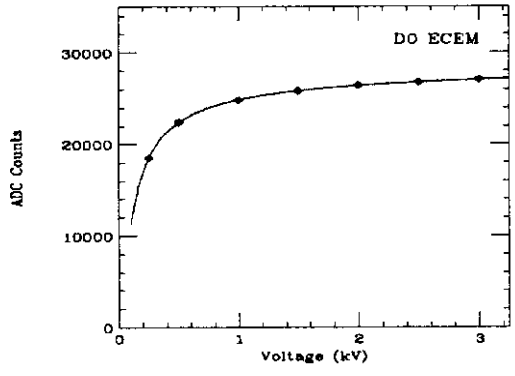

Figure 5. High voltage plateau curve for the EC EM module, using test beam electrons. Our operating voltage is 2 kV.

The response to electrons as a function of the beam momentum for both CC and EC is shown in Fig. 6. Plotted on the y-axis is the difference between the reconstructed calorimeter energy (as given by Eq. 2) and the incident beam momentum, normalized to the beam momentum. (More low energy data was taken during the CC test, which accounts for the relative preponderance of points below 10 GeV in the upper plot.) We measure an electron response that is linear to better than 1% for energies between 10 and 150 GeV in both the CC and EC. We do find, however, non-linearities at the few hundred MeV level for electrons with energies between 3 and 10 GeV. The reproducibility of this non-linearity *in situ* is being investigated using the masses of reconstructed low energy resonances – the J/ψ, π^0, and the Υ.

The resolution as a function of incident beam momentum for electrons and pions in both the

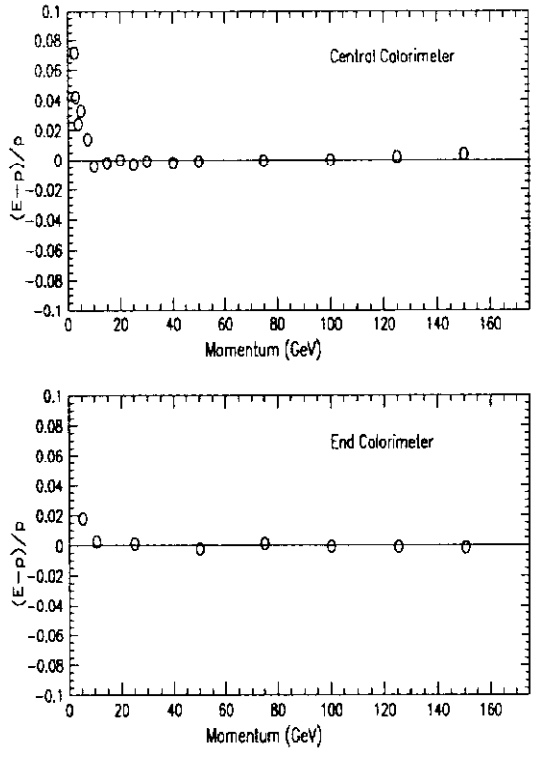

Figure 6. Response of the calorimeter to electrons as a function of the incident beam momentum for both CC and EC, as measured at the test beam. *(DØ Preliminary)*

CC and the EC is shown in Fig. 7. We fit these curves to the functional form:

$$\left(\frac{\sigma}{E}\right)^2 = \left(\frac{N}{E}\right)^2 + \frac{S^2}{E} + C^2, \qquad (3)$$

where N, S, and C are the noise, sampling, and constant terms, respectively. (The beam energy, E, is in GeV.) For electrons, we have found a 14.8 (15.7)% sampling term in the CC (EC), and a small associated constant term (0.3% in both CC and EC). Fits to the pion resolution curves yield sampling terms of 47.0 (44.6)%, and constant terms of 4.5 (3.9)% for CC (EC).

Our results for the electron to pion response ratio (e/π ratio) are shown in Fig. 8, along with a GEANT [6] Monte Carlo simulation incorporating the GHEISHA [7] shower program. Shown is

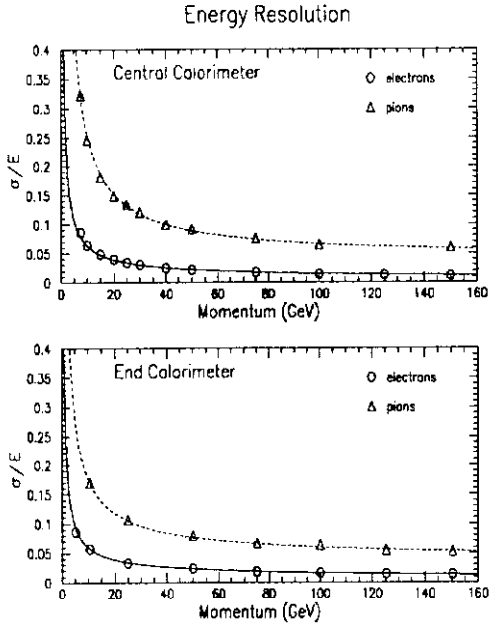

Figure 7. Energy resolution as a function of beam momentum, obtained from the test beam, for both electrons and pions in both the CC and EC. The fits are described in the text. *(DØ Preliminary)*

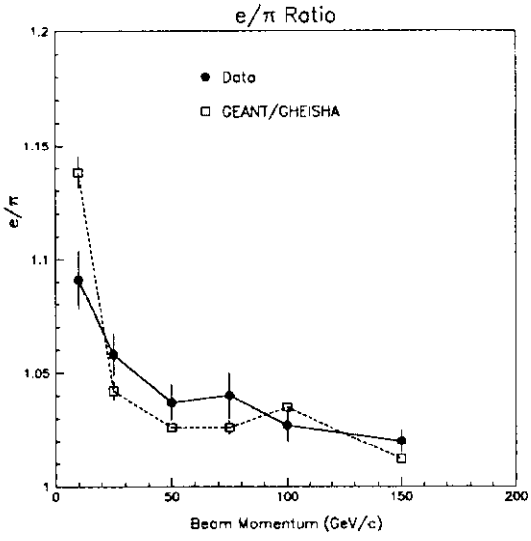

Figure 8. Ratio of electron to pion response in the EC electromagnetic/inner hadronic module combination. Both test beam data and results of a Monte Carlo simulation are shown.

the e/π ratio as determined from the measured response of electrons and pions incident on the EC electromagnetic and inner hadronic module combination. Corrections for the energy lost outside the $\Delta\eta \times \Delta\phi$ cone used to define the particle shower, event pileup, and early showering have been applied. The e/π ratio varies from $\approx$ 1.09 at 10 GeV to $\approx$ 1.02 at 150 GeV.

The position resolution in r-ϕ as a function of beam energy for electrons at a fixed impact point in the end calorimeter EM module is shown in Fig. 9. An energy-weighted centroid at shower maximum (EM layer 3) is used to determine the shower position in the calorimeter, which is compared to the position of the track as determined from proportional wire chambers that define the beam direction. The resolution for tracks that impact the edge of a tower, and that for tracks where no such restriction is imposed, are shown. In either case, the resolution is better than $\approx$ 2 *mm* for electron energies greater than 20 GeV.

We have also studied the module uniformity at the test beam. The EC EM module has been shown to have a uniform response in both r-ϕ and η to $\approx$ 0.4% (*r.m.s.*). The two CC EM modules that were tested showed variations of $\approx$ 2-3%, peak-to-peak, in both η and ϕ[1]. Although these response non-uniformities in the CC are larger than we would have liked, they are being addressed in detail by *in situ* studies, and are discussed in later sections. These non-uniformities also impact the absolute energy scale carried over from the test beam, which is discussed in the following section.

[1]It will be recalled that, for CC, variations in ϕ correspond to variations from module-to-module, while those in η at fixed ϕ reflect variations from tower-to-tower within a module.

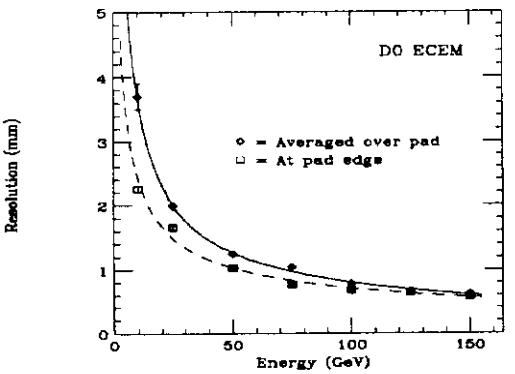

Figure 9. Position resolution in r-ϕ as a function of beam energy for electrons in the EC EM section. The solid (dashed) line is a fit to the data using a functional form of 16.6 $mm \times E^{-0.66}$ (8.2 $mm \times E^{-0.53}$), where E is the shower energy in GeV.

3.3. Transfer of absolute calibration from test beam

One of the primary difficulties of dealing with a liquid argon system is the large cryogenic system it requires. This imposes a significant restriction on the logistics of a test beam calibration scheme: the size and complexity of the cryogenics, necessarily long cool-down times, and other aspects of module testing dictate that only a subset of the modules can be tested. For *in situ* measurements, we apply our knowledge of material composition and thickness throughout the detector, measured during module construction, to put all regions of the calorimeter on an equal response footing. In principle, one overall constant, converting ADC counts to GeV, is then applied to establish the proper EM scale for the entire device. (In practice, this procedure is performed independently for the CC and the EC's.) The carry-over of a calibration from the test beam intrinsically assumes that the subset of tested modules can be put on the same footing as those in the main experiment, to the desired level of accuracy.

The CC modules tested in the test beam consisted of a set of spare modules that were no different mechanically from those installed in the final experiment – they were, in effect, chosen at random, with the absolute scale for the CC EM established by performing energy scans of one of the two EM modules that were beam tested. Given the 2-3% response variations quoted above, it is clear that one can reasonably expect errors of this order when applying the calibration constant derived from the "calibration module" to any of the others. The validity of the calibration constant when applied to the collider data obtained in the final experiment clearly depends on where the "calibration module" sits in the response hierarchy of the 32-module CC array. The inclusion in the final array of the CC EM module that was used for the test beam calibration would have allowed us to establish its response relative to the other 31 modules.

It was an unfortunate fact, however, that scheduling constraints prohibited us from putting any of the CC modules that were beam tested into the final experiment – the test beam and installation of the central calorimeter took place concurrently. Without this, there is no way to satisfactorily anchor the test beam calibration in the final experiment, and the response variations have to be subsumed into the error in the calibration transfer. For the EC, we were able to test and calibrate the south end calorimeter EM module directly. The north EC EM module was being installed during the beam test, and so could not be tested.

The initial indication of the accuracy with which the calibration was transferred from the test beam to DØ was obtained from the reconstruction of the $Z \rightarrow ee$ resonance. The dielectron invariant mass peak obtained *in situ* from 13.9 pb^{-1} of data is shown in Fig. 10. Both electrons were required to be in the central calorimeter. The test beam calibration constants and sampling weights – α, β_j, and δ resulting from the analysis described in Section 3.1 – were used to establish the electron energies. Overlayed on the left-hand plot is a fit to a Breit-Wigner form, convoluted with a Gaussian to simulate the pedestal widths and detector resolution. A linear function is used to simulate the Drell-Yan background. The negative log likelihood as a function of the mass is shown in the right-hand plot, which yields

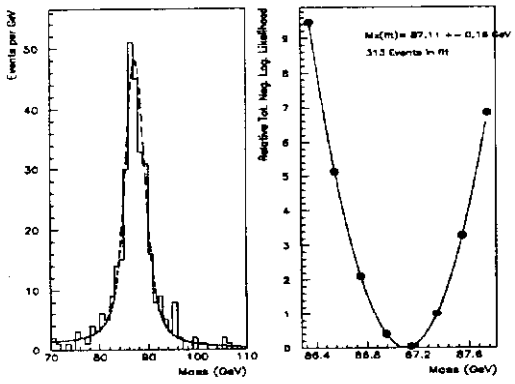

Figure 10. Plot of invariant mass of Z candidate events in central calorimeter, along with a negative log likelihood fit to the data. *(DØ Preliminary)*

a fitted Z mass of 87.11 ± 0.18 GeV. The same technique was used to obtain the Z masses in both of the end calorimeters.

Table 2 shows the ratio of the invariant mass of the Z boson obtained from the LEP experiments at CERN [8] to that obtained at DØ, using the nominal test beam calibration, for each of the three cryostats. The first error represents the statistical and systematic error associated with the *in situ* analysis (added in quadrature), while the second error is due to the calibration transfer. The transfer error is dominated by the uncertainty in the liquid argon purity ($\approx 1.5\%$) and, for CC, the module-to-module non-uniformity (1.4%). The means by which we obtain this latter error is discussed in detail in section 4.2.

It is worthwhile to note that the test beam calibration was used primarily for the initial shakedown and running in collider mode. Our energy scale has ultimately been set by calibrating to the Z resonance. The numbers shown in Table 2 represent the scale factors used to establish our electromagnetic energy scale in the three cryostats – the energies of electrons and photons are multiplied by the factors shown in order to properly set the energy scale in the calorimeters. Other aspects of our *in situ* calibration will be discussed in later sections.

Table 2
Results from the test beam calibration

Cryostat	$M_Z^{LEP}/M_Z^{DØ}$
CC	$1.047 \pm 0.002 \pm 0.020$
EC North	$1.035 \pm 0.011 \pm 0.016$
EC South	$1.005 \pm 0.011 \pm 0.018$

4. PERFORMANCE IN THE COLLIDER

DØ has been running in the collider for almost three years, with the fully-assembled detector placed in its final position in the collider hall in February, 1992. We discuss below first the stability and reliability of the system, followed by a discussion of our *in situ* means of more extensively probing the electromagnetic calibration of the central calorimeter. We end this section with a brief description of how we establish our jet energy scale.

4.1. Stability and reliability

Of the 47,800 channels in the three calorimeters, we find fewer than 10 (or 0.02%) to be inoperative, on average, at any given time. These are typically failed preamplifier or shaper hybrids that are replaced when an accelerator down-time allows us to access the detector. The integrated number of failed channels from January–October, 1994 is given in Table 3.

In order to monitor closely the baseline of the electronics, pedestal runs are taken as often as possible during collider running. The frequency with which these runs are taken is determined by accelerator live time (pedestal runs require that

Table 3
Electronics reliability from January through October, 1994

Channel Type	Failures/Total	Failures(%)
ADC	3/3,456	0.1
Shaper	153/47,800	0.3
Shaper drivers	3/3,456	0.1
Preamplifier	3/47,800	< 0.01
Power supplies	0/73	0

there be no beam in the Tevatron), and turns out to be at least three or four times per week. We have found the mean pedestal value for the detector, defined to be the mean of all 47,800 pedestal means, to be stable to ≈ 0.1 ADC counts over an eight month period (February–September, 1994).

In order to equalize the gains for all of the electronics channels (making them independent of cell capacitance), DØ employs a precision calibration pulser that injects charge directly at each preamplifier input. The pulser also monitors, and permits a correction for, any time dependence in the response of the electronics chain to charge in the system. Pulser runs are taken approximately three times per week. We have found the electronics gains, as measured by the calibration pulser (and defined in an analogous way as the pedestals), to be stable to $\approx 0.2\%$ over the same time period.

We have placed test cells containing radioactive α sources, to monitor the stability of the argon's response to heavily-ionizing particles, and β sources, to monitor the response to minimum-ionizing particles, at three different elevations in each of the three cryostats. Figure 11 shows the response of the α cells at the equator of each of the cryostats over a ten month period (November, 1993 – August, 1994). We find from these data that the loss of response to heavily-ionizing particles is less than $\approx 0.5\%$ per year. Analogous plots for the β sources show that, at the $\approx 1\%$ level, there is no measurable degradation in the response to minimum-ionizing particles. From shape analyses of the high voltage plateau curves for the β sources in CC, we have measured an absolute purity of 0.25 ± 0.01 parts-per-million oxygen equivalent. Similar absolute purity levels have been measured in the end calorimeters.

4.2. Relative calibration of EM section

Test beam results previously described have indicated that we might expect response variations at the few-% level in the CC EM section. This has helped to motivate an *in situ* study of the relative response of the CC EM modules [9]. The goal of this work was to equalize the average response for all 32 modules. The method exploits the ϕ-symmetry of E_T flow at the collider, and has

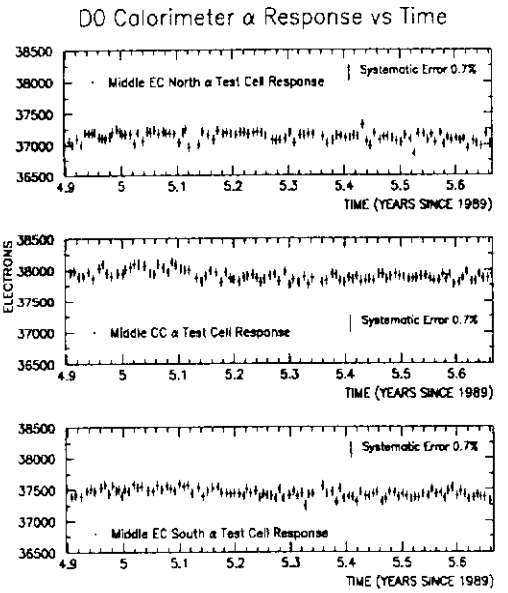

Figure 11. Stability of response to heavily-ionizing sources in the three cryostats. The time scale spans 11 months. *(DØ Preliminary)*

therefore come to be called the ϕ-uniformity calibration. A similar analysis for the end calorimeters is in progress.

The method assumes that the measured E_T and the true E_T in the i^{th} module differ from one another solely by a multiplicative constant; i.e., that there is no additive offset:

$$E_T^i(\text{true}) = \gamma^i E_T^i(\text{measured}). \qquad (4)$$

We call the γ^i the calibration constants. Using electromagnetic triggers at low E_T thresholds in order to maximize statistics, we find the γ^i for which the number of events with E_T(true) greater than some threshold E_T is the same in each module. Figure 12 shows the value of the calibration constants obtained. The upper plot shows the γ^i in each of the 32 modules (each EM module in CC subtends 0.2 radians in azimuth). The error on each of the data points is $\approx \pm 0.5\%$, approximately equal to the size of the data points. The lower plot shows a histogram of the 32 values; the *r.m.s.* of the distribution is 1.4%. Since these

numbers are only applied in an effort to obtain a relative calibration, the mean value for the calibration constants has been set equal to unity. All modules are then scaled up together to the value determined by the Z resonance.

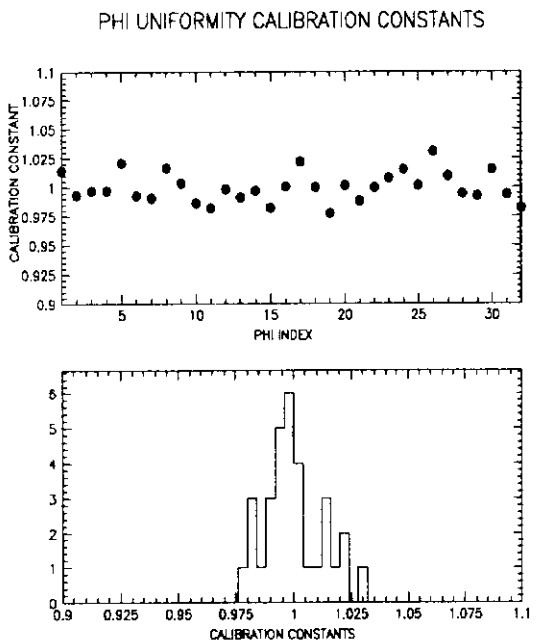

Figure 12. Module-to-module calibration constants obtained *in situ* for the CC EM section. *(DØ Preliminary)*

To verify the efficacy of the procedure used to derive the γ^i, we have applied the above calibration constants to $W \rightarrow e\nu$ events. We classify the modules into three groups: those that lie in the lowest ($\gamma < 0.99$), middle ($0.99 < \gamma < 1.01$), and uppermost ($\gamma > 1.01$) regions of the response hierarchy as dictated by the magnitude of the calibration constants shown in Fig. 12. We obtain the W transverse mass distribution in each of the three groups, both before and after the electron energy is scaled by the calibration constant which corresponds to the module it has traversed. The W masses, extracted from a fit to each transverse mass distribution, are plotted in Fig. 13. It is clear that the W masses in the three groups of modules agree far better after application of the calibration constants. This and other checks have helped convince us that the calibration constants obtained as described above accurately reflect the module-to-module gain variations, and are not the result of some artifact of the technique used to obtain them.

Clearly, this analysis needs to be done in the η coordinate as well. In order to obtain a result of adequate statistical power ($< 0.5\%$ error), a large data set is required. These data are in the process of being recorded and analysed.

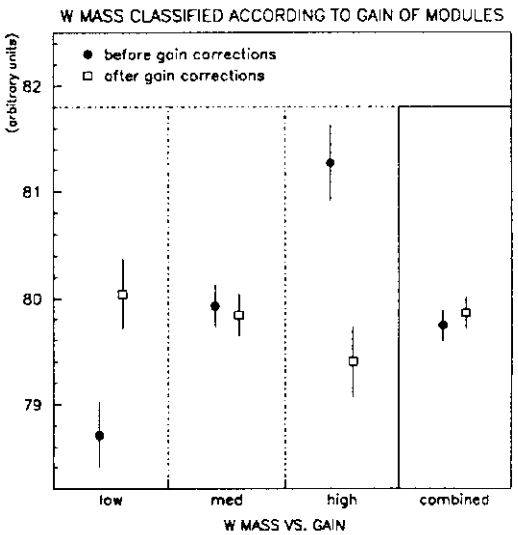

Figure 13. W mass obtained in the CC before (closed circles) and after (open squares) applying the ϕ-uniformity calibration constants. Units on the vertical axis are arbitrary. Errors are statistical only. *(DØ Preliminary)*

4.3. Evaluation of the offset *in situ*

Of fundamental concern in scaling the energy from the test beam value is the error that the procedure incurs. This is of particular importance in the measurement of the W mass, where the error in the energy scale is the largest systematic uncertainty. A major component of this scale error is determined by the magnitude of the error on

the additive offset assumed to exist in the relation between the true and the measured electron energies at DØ.

We use a technique that has come to be called the "binned Z" method in order to evaluate the offset *in situ* [10]. The approach exploits the fact that the electrons resulting from $Z \rightarrow ee$ decays are not monochromatic: their energies range from $\approx$ 25 to 80 GeV in the CC. The following functional form is assumed for the true electron energy:

$$E^e(\text{true}) = \kappa E^e(\text{meas}) + \rho. \quad (5)$$

Here, κ and ρ are the scale factor and offset, respectively, and $E^e(\text{meas})$ ($E^e(\text{true})$) is the measured (true) electron energy. We apply the standard formula for the invariant mass:

$$M^2_{inv} = 4E^e_1 E^e_2 \sin^2\left(\frac{\omega}{2}\right), \quad (6)$$

where $E^e_{1,2}$ is the energy for the first/second electron, and ω is the opening angle between the two electrons. Substituting Eq. 5 into Eq. 6 and expanding around $\rho = 0$, we obtain:

$$M^{ee}(\text{true}) = \kappa M^{ee}(\text{meas}) + f\rho, \quad (7)$$

where f is a factor determined purely from the kinematics of the decay:

$$f = \frac{2\left(E^e_1(\text{meas}) + E^e_2(\text{meas})\right)}{M^{ee}(\text{meas})} \sin^2\left(\frac{\omega}{2}\right). \quad (8)$$

We can express Eq. 7 in the following more useful form:

$$M^{ee}(\text{meas}) = \left(-\frac{\rho}{\kappa}\right) f + \frac{M^{ee}(\text{true})}{\kappa}. \quad (9)$$

Plotting $M^{ee}(\text{meas})$ against (the measured quantity) f allows us to extract both κ and ρ. Figure 14 shows a plot of $M^{ee}(\text{meas})$ vs. f in the CC. From the slope and offset of the fitted line, we obtain values of 1.050 ± 0.015 and -320 ± 780 MeV for κ and ρ, respectively.

Additional measurements of the offset ρ are obtained *in situ* using low energy resonances [11]. Applying information obtained from both the decay kinematics and the masses of the J/ψ and π^0, in conjunction with those from the Z, values for ρ can be extracted for each.

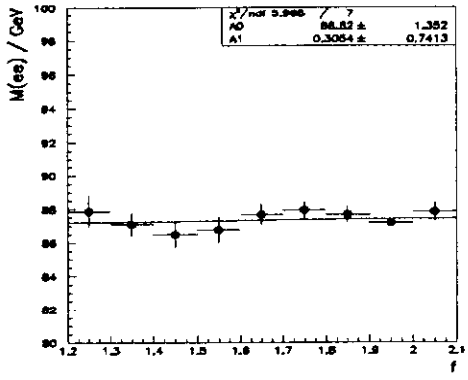

Figure 14. Plot of $M^{ee}(\text{meas})$ vs. f for electrons from Z decay in the CC. *(DØ Preliminary)*

Table 4 shows the offsets we obtain for each of the three methods. All three values are consistent with one another, within errors. We are currently in the process of adding the Υ resonance to this list.

Table 4
Offsets measured *in situ*

Method	Offset ρ (MeV)
Binned Z	-320 ± 780
J/ψ	-130 ± 410
π^0	-245 ± 314

As already mentioned, the above work is motivated primarily by our desire to establish (and contain) the scale error on the W mass. At present, we are using the uncertainty on ρ of 780 MeV as obtained from the "binned Z" method to compute this error. Use of this value results in a scale error on the W mass of 260 MeV.

4.4. Jet Calibration

The most reliable means of calibrating the hadronic energy scale comes from *in situ* measurements. The low-energy pion beam at the test beam was of sufficiently poor quality that application of the information at DØ has proven to be of limited use. *In situ* probes of the hadronic

scale have proven to be far more reliable[2].

The primary ingredient in the calibration of the hadronic scale is derived from "γ"+1 jet processes that are restricted to the central calorimeter. (The "γ"'s in this context are mostly π^0's). The hadronic scale in the CC is calibrated relative to our known electromagnetic scale, as described below.

The method assumes that the $\not\!\!E_T$ in such events results predominantly from the jet/"γ" response imbalance. Since the jet/"γ" final state consists of two bodies, and one expects the jet response to be lower (on average) than the electromagnetic response, we anticipate that the $\vec{\not\!\!E}_T$ will point predominantly in the transverse direction of the jet. The component of $\vec{\not\!\!E}_T$ in the transverse direction of the photon, therefore, will be (again, on average) a negative quantity, that represents a measure of the response deficiency of jets with respect to highly electromagnetic objects.

Expressing the above mathematically, we take the response of the calorimeter to hadrons, R_{had}, to be given by:

$$R_{had} = 1 + \frac{\vec{\not\!\!E}_T \cdot \hat{n}_T^\gamma}{E_T^\gamma}, \qquad (10)$$

where E_T^γ is the transverse energy of the photon, and $\hat{n}_T^\gamma$ is the unit vector along the photon direction in the plane transverse to the beam axis. (It will be recalled that the $\not\!\!E_T$ is defined only in the transverse plane.) The quantity represented by the quotient on the right hand side of Eq. 10 therefore represents the component in this plane of the $\vec{\not\!\!E}_T$ along the transverse direction of the photon, normalized to the total photon E_T.

The lack of statistics for these types of events in the forward regions, particularly at high E_T, allows us to apply this procedure only in the central region. Having obtained the hadronic scale in the central calorimeter by the above method, the calibration is propagated to the end calorimeters using dijet events, in which one jet is required to be confined to the CC.

The full jet correction is given by the following formula:

$$E(\text{meas}) = (1 - C)\, R_{had} E(\text{true}) + U, \qquad (11)$$

where U represents the energy contributed by both the underlying event and the suppression of our asymmetric pedestals, and C represents unseen energy resulting from limitations in the algorithm used to define the jet. The quantities E(true) and E(meas) denote the true and measured jet energies, respectively. All three of the quantities in Eq. 11 – R_{had}, U, and C – depend on E(true), η and ϕ, while C and U depend on the algorithm used as well.

The full jet correction as a function of the jet transverse energy for two different η positions is shown in Fig. 15. The corrections shown were determined for jets that were identified using a fixed cone algorithm of half-angle $R = 0.7$, where $R = \sqrt{(\Delta\eta)^2 + (\Delta\phi)^2}$. The ordinate represents the factor by which measured jet energies are multiplied in order to obtain the true jet energy. The average correction for $E_T > 20$ GeV is approximately 15-25%, with an error of about $\pm 5\%$.

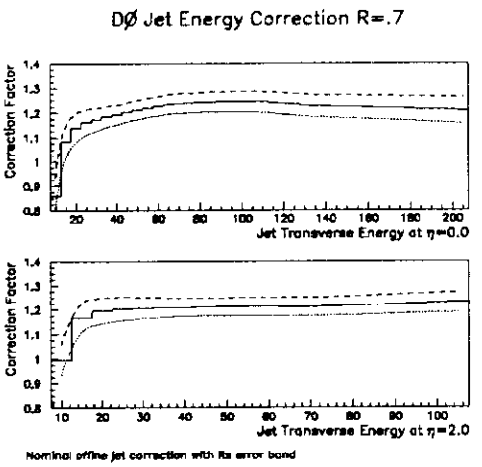

Figure 15. Full jet energy scale correction as a function of the jet transverse energy for two different η positions, with its error band. The correction was derived from jets that were identified using a fixed cone algorithm of half-angle $R = 0.7$. *(DØ Preliminary)*

[2]For details on our identification and calibration of jets, the reader is directed to Ref. [12].

An example of the physics that hermetic, homogeneous detection of jets enables us to pursue is shown in Fig. 16, which is a plot of the inclusive differential dijet cross section. One jet is required to be central ($|\eta_1| < 1.0$), and the cross section is plotted as a function of the E_T of this jet for various η ranges of the second jet (η_2). The pseudorapidity of the second jet extends to $|\eta_2| = 4$. The data are compared to a next-to-leading order prediction that incorporates CTEQ2M parton distribution functions and the parton-level event generator JETRAD [13–15]. This analysis is one of many where we exploit the full coverage and large dynamic range of the calorimeter: tests of quantum chromodynamics over a broad range of both pseudorapidity and jet E_T are major portions of the physics program at DØ.

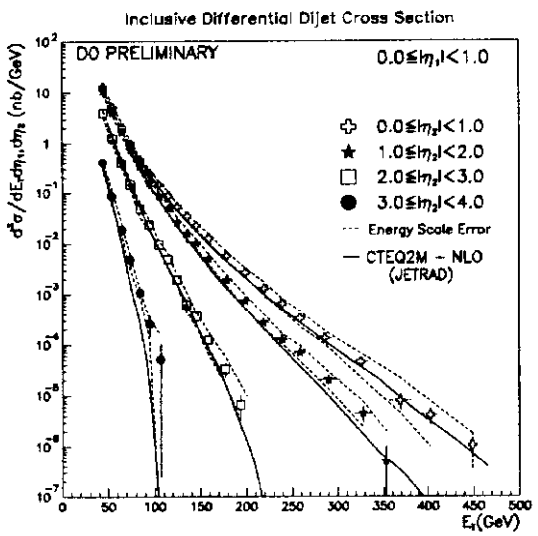

Figure 16. Inclusive differential dijet cross section. The jet energy scale uncertainty is given by the dotted lines. An additional 12% error, due to the uncertainty in the integrated luminosity, is not included. *(DØ Preliminary)*

5. CALORIMETER UPGRADE

With completion of the Main Injector at Fermilab's Tevatron at the end of 1998, the instantaneous luminosity of the delivered beams is expected to increase by about an order of magnitude with respect to its current value of $\approx 10^{31}\ cm^{-2}$-sec^{-1}. Along with this luminosity increase, the bunch crossing time will be going from its present value of 3.5 μs to either 396 ns or 132 ns. Of most significance for the upgrade of the calorimeter is that the cryostats are welded shut and will not be changed internally; this places all of the burden for the calorimeter upgrade on the readout electronics.

A few of our design goals for the upgrade are enumerated below:

- With faster detector readout, the random noise due to uranium decays decreases, but the electronics noise increases. At higher luminosities, the noise due to pile-up increases as well. Our goal for the upgrade is to keep the total noise at the preamplifier output approximately the same as it is now.
- We would like to keep the coherent noise at or below current levels, despite the faster shaping time.
- The dynamic range will be kept at 15 bits.
- Currently, we have a precision pulser that is used to correct for the intrinsic $\approx$ 20% channel-to-channel gain variations. (These variations are primarily due to the spread in capacitance at the preamplifier inputs.) The goal for the upgraded system is to achieve a $\approx$ 5% relative calibration prior to any pulser corrections.
- We must be able to store the calorimeter data from every 132 ns crossing while awaiting the return of a decision from our hardware trigger. This (irreducible) delay, which is dominated by cable lengths, is $\approx 2.3\ \mu s$.

We are replacing all of the existing 47,800 preamplifiers with a lower noise "dual FET" version, that has its input impedance matched to that of the input cables in order to minimize reflections. The preamplifier hybrid also performs a pole-zero compensation, which equalizes the rise times between channels of different

capacitance. Due to the short shaping times, channel-to-channel variations between the time when charge is deposited in the detector and the time when it reaches the preamplifier input can also cause significant response variations. In an effort to minimize this effect, we are equalizing the cable lengths between the calorimeter cell and the preamplifier input by adjusting the cable lengths external to the cryostat but upstream of the preamplifiers.

Downstream of the preamplifiers, we are introducing a Sallen-and-Key filter [16] for signal shaping, with ≈ 400 *ns* peaking time, in order to minimize the effects of pileup. Given the shorter bunch spacing, some method of storing the data while the trigger decision is being made is a necessity. We will employ switched capacitor arrays (SCA) for analog data storage. There are two SCA channels per input channel, allowing for the contents of one to be read out while the other is being filled. Each SCA channel is 48 buffer-channels deep, allowing for storage of multiple events prior to receipt of the trigger decision.

6. CONCLUSIONS

DØ has a hermetic, smoothly-functioning uranium/liquid argon calorimeter with good energy resolution and linearity, and broad dynamic range. Extensive studies of calorimeter modules in test beams have shown that most of our design goals have been realized in practice, with some excellent results. Stable and reliable operation of the full calorimeter *in situ* has been seen for over two years, with excellent argon purity profiles and electronics performance. Our electromagnetic energy scale has been calibrated *in situ* using the Z resonance; additional features of our energy scale are being probed using information extracted from low-energy resonances. The scheme for the upgrade has been determined, with a test of the first 5,000 channels scheduled for the summer of 1995.

DØ is pursuing a full physics menu, and expects to record ≈ 100 pb^{-1} of data prior to the shutdown to install the upgraded detector (December, 1995). We look forward to an exciting and productive physics program during the coming decade.

REFERENCES

1. The pseudorapidity, η, is defined by the relation $\eta \equiv -\ln[\tan(\theta/2)]$, where θ is the polar angle with respect to the proton-beam direction.
2. S. Abachi *et al.*, *Nucl. Instr. Meth.* **A338** (1994) 185.
3. H. Aihara *et al.*, *Nucl. Instr. and Meth.* **A325** (1993) 393.
4. J. Guida, *Proceedings of the* 3^{rd} *International Conference on Calorimetry in High Energy Physics*, Corpus Christi, Texas, September 29-October 2, 1992, p. 465.
5. J. Kotcher, Ph.D. Thesis, New York University, New York, New York (October, 1992) (DØ Internal Note DØ-1507).
6. R. Brun *et al.*, CERN-DD/EE/84-1 (1986).
7. H. Fesefeldt, RWTH Aachen report RWTH/PITHA 85/02.
8. D. Schaile, presented at the 27^{th} *International Conference on High Energy Physics*, Glasgow, Scotland (July, 1994), CERN-PPE-94/162.
9. Q. Zhu, Ph.D. Thesis, New York University, New York, New York (April, 1994) (DØ Internal Note DØ-2160).
10. U. Heintz, DØ Internal Note DØ-1819, (July, 1993).
11. U. Heintz, DØ Internal Note DØ-2209, (July, 1994); U. Heintz, DØ Internal Note DØ-2268 (August, 1994); I. Adam, DØ Internal Note DØ-2298 (October, 1994).
12. H. Weerts, *Proceedings of the* 9^{th} *Topical Workshop on Proton-Antiproton Collider Physics*, University of Tsukuba, Ibaraki, Japan, October 18-22, 1993, p. 192.
13. W.T. Giele, E.W.N. Glover, and D.A. Kosower, *Nucl. Phys* **B403** (1993) 633-667.
14. J. Botts *et al.*, *Phys. Lett.* **B304** (1993) 159.
15. W.T. Giele, E.W.N. Glover, and D.A. Kosower, FERMILAB-Pub-94/070-T (1994).
16. P. Horowitz and W. Hill, *The Art of Electronics*, 2^{nd} ed., Cambridge University Press, 1989, p. 267.